

Disentangling representations in Restricted Boltzmann Machines without adversaries

Jorge Fernandez-de-Cossio-Diaz,* Simona Cocco, and Rémi Monasson
*Laboratory of Physics of the Ecole Normale Supérieure,
 CNRS UMR 8023 & PSL Research, Sorbonne Université, Paris, France*
 (Dated: June 24, 2022)

A goal of unsupervised machine learning is to disentangle representations of complex high-dimensional data, allowing for interpreting the significant latent factors of variation in the data as well as for manipulating them to generate new data with desirable features. These methods often rely on an adversarial scheme, in which representations are tuned to avoid discriminators from being able to reconstruct specific data information (labels). We propose a simple, effective way of disentangling representations without any need to train adversarial discriminators, and apply our approach to Restricted Boltzmann Machines (RBM), one of the simplest representation-based generative models. Our approach relies on the introduction of adequate constraints on the weights during training, which allows us to concentrate information about labels on a small subset of latent variables. The effectiveness of the approach is illustrated on the MNIST dataset, the two-dimensional Ising model, and taxonomy of protein families. In addition, we show how our framework allows for computing the cost, in terms of log-likelihood of the data, associated to the disentanglement of their representations.

I. INTRODUCTION

Unsupervised learning involves mapping data points to adequate representations, where the statistical features relevant to the data distribution are encoded by latent variables [1]. Examples of unsupervised architectures include restricted Boltzmann machines [2], variational auto-encoders [3], and generative adversarial networks [4], among others. However, the mapping between latent-variable activities and the relevant properties of the data is generally complex and not easily interpretable (Figure 1), a phenomenon referred to as *entanglement* of representations in machine learning, or mixed sensitivity in computational neuroscience [5]. Entangled representations are hard to interpret and to manipulate, e.g. for generating new data with desired properties [1, 6].

A stream of literature has recently focused on how to train unsupervised models to obtain disentangled representations, where information about certain properties are concentrated in some latent variables and excluded from others [7–13], or absent altogether from representations [14, 15]. Concentration of information makes, in turn, possible to change the values of few variables and generate data points with controlled properties [7]. In practice, learning of disentangled representations is often done in an adversarial framework through optimization of variational bounds to quantities hard to estimate, such as mutual information between the data features and some part of the representations. While conceptually appealing, this approach may be tricky to adopt from a numerical point of view, due to well-known difficulties in adversarial-based learning [16]. In addition, its complexity has prevented theoretical analysis so far, leaving important questions, such as the cost of disentangling representations unanswered.

The purpose of the present work is to propose a method for disentanglement of representations, which is both effective on real data and amenable to mathematical analysis. We consider Restricted Boltzmann Machines (RBM), a simple unsupervised generative model implementing a data/representation duality [17]. RBMs are used as building bricks of deeper networks [2], and are competitive with more complex models in various relevant situations [18–20]. We derive conditions on the RBM parameters, which deprive all or part of the representation from information about data labels. This procedure allows us to concentrate the information about labels into a subset of latent units. Manipulation of these units then allows us to generate high-quality data with prescribed label values. Furthermore, the simplicity of our framework allows us to estimate the loss in log-likelihood resulting from the disentanglement requirement, with a deep connection with Poincaré separation theorem [21]. Informally speaking, this loss is the cost to be paid for enhanced interpretability of the machine.

Our paper is organized as follows. We first show that standard learning with RBM generically produces entangled representations on three applications, chosen for their diversity and interest: (1) the MNIST dataset of handwritten digits [22], where the digits represented in each image are the labels; (2) the two-dimensional Ising model, where configurations are annotated by the sign of their magnetizations; (3) protein sequence families from the PFAM database [23] annotated based on their taxonomic origins. We then present how our approach learns disentangled representations, and demonstrate its effectiveness when applied to the three data distributions listed above. Special emphasis is brought to the physical meaning of the unsupervised models corresponding to the Ising model case. We then calculate the costs associated to representation disentanglement.

* j.cossio.diaz@gmail.com

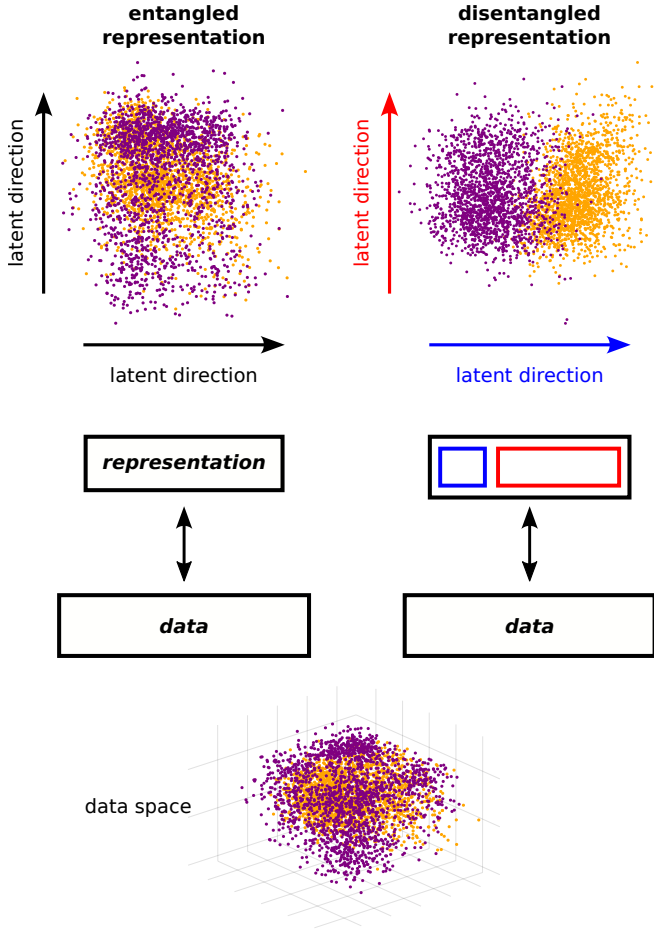


FIG. 1. **Entangled vs. disentangled representations.** A set of high-dimensional data points (bottom) is mapped, through unsupervised learning onto latent representation (top). Data are colored in purple and orange according to a binary-valued property, e.g. being an odd or even number for MNIST images of handwritten digits. Left: When representations are *entangled*, the separation of data classes is not aligned with a single latent direction. Right: When representations are *disentangled*, one or few directions in latent space (blue) separate the labeled classes, while other directions are not correlated with the label (red).

II. REPRESENTATIONS OF COMPLEX DATA WITH RESTRICTED BOLTZMANN MACHINES ARE GENERALLY ENTANGLED

A. Unsupervised learning with RBM

Restricted Boltzmann Machines (RBM) are bipartite graphical models over N visible variables $\mathbf{v} = \{v_1, v_2, \dots, v_N\}$ and M hidden (or latent) variables $\mathbf{h} = \{h_1, h_2, \dots, h_M\}$, see Figure 2A. Both visible and hidden variables are assumed to be Bernoulli, *i.e.* to take 0 or 1 values. The two layers are connected through the interaction weights $w_{i\mu}$. An RBM defines a joint probability

distribution over \mathbf{v} and \mathbf{h} through

$$P(\mathbf{v}, \mathbf{h}) = \frac{1}{Z} e^{-E(\mathbf{v}, \mathbf{h})}, \quad (1)$$

where Z is a normalizing factor and the energy E is given by

$$E(\mathbf{v}, \mathbf{h}) = - \sum_{i=1}^N g_i v_i - \sum_{\mu=1}^M \theta_{\mu} h_{\mu} - \sum_{\mu=1}^M I_{\mu}(\mathbf{v}) h_{\mu} \quad (2)$$

The parameters g_i and θ_{μ} are local fields biasing the distributions of single units, and

$$I_{\mu}(\mathbf{v}) = \sum_{i=1}^N w_{i\mu} v_i \quad (3)$$

is the input received by hidden unit μ given the visible configuration.

Marginalizing over the states of the hidden units results in the likelihood $P(\mathbf{v}) = \frac{1}{Z} \sum_{\mathbf{h}} e^{-E(\mathbf{v}, \mathbf{h})}$ of visible configurations that can be fit to data. Given a set of data points \mathcal{D} , the weights and potential-defining parameters of the RBM are learned through gradient ascent of the dataset log-likelihood,

$$\mathcal{L} = \langle \log P(\mathbf{v}) \rangle_{\mathcal{D}}, \quad (4)$$

where the average $\langle \cdot \rangle_{\mathcal{D}}$ is taken over the data points. In practice computing the gradient of \mathcal{L} requires to estimate the moments of visible and/or hidden variables with respect to the model distribution [17]. Regularization of the weights can also be easily included in this approach. Details about the computation of the gradient and the training procedure implemented in this work can be found in Supplementary Material.

B. Datasets

We train the RBM on three datasets, illustrated by the three columns in Figure 2B:

1. MNIST handwritten digits

The MNIST dataset [22] consists of a collection of 70,000 images of 28×28 pixels each, labeled by the identity of the 0-9 handwritten digit they represent. We show 16 of them in Figure 2B. We hereafter consider in particular (1) *MNIST0/1*, a simplified version of MNIST consisting only of images of the digits 0 and 1, with binary labels $u = 0, 1$; and (2) *MNIST0/1/2/3*, the set of all images of digits from 0 to 3, with 4-state labels u .

2. Two-dimensional Ising model

As a second example, we consider the Ising model [24] on a two-dimensional regular square grid, with uniform

positive interactions between nearest-neighbour spins. The values of the interaction, or, equivalently, of the inverse temperature are varied to explore both paramagnetic (weak interactions) and ferromagnetic (strong interactions) regimes. Each configuration is labeled according to the sign u of its magnetization m , *i.e.* the differences between the numbers of + (black dots in Figure 2B) and - spins (white dots).

3. Pfam database of protein family sequences

Last of all, we consider protein families in the PFAM sequence database [23]. A protein family consists of a collection of homologous protein sequences from different organisms, *i.e.* sharing common evolutionary origins and common functional or structural features. As an illustration Figure 2B sketches some sequences of the K homology domain found in nucleic-acid binding proteins. Many families include sequences issued from prokaryotic and eukaryotic organisms, and we use this classification as the label u for sequences in the dataset.

C. RBMs learn distributed representations of the label

Although a precise definition of disentangled representation learning is debated [6, 13], some desirable properties are agreed upon [1]. Ideally, interesting features map to single dimensions in latent space, which can then be manipulated to affect a property of interest in data space (Fig. 1).

We assess the ability of RBM to produce disentangled representations in our datasets. We trained RBMs with 200 - 400 binary hidden units (see Supplementary materials for details) on MNIST0/1, the 2-dimensional Ising model, and the KH domain protein family. Consistent with previous results on related datasets [18, 19, 25, 26], RBM accurately fit and generate high-quality samples in the three cases (illustrated Figure 2C). In addition, training simple classifiers to predict the label from the hidden inputs of the models, gives an area under the curve (AUC) of > 0.9 in all cases (see Supplementary materials), demonstrating that the RBM automatically captures information relevant to the label. We emphasize that in all cases the RBM does not see the label during training. Next, we plot in panel 2D the histogram of correlations between the label and hidden unit inputs, defined by

$$C_\mu = \langle u(\mathbf{v}) I_\mu(\mathbf{v}) \rangle_{\mathcal{D}} - \langle u(\mathbf{v}) \rangle_{\mathcal{D}} \langle I_\mu(\mathbf{v}) \rangle_{\mathcal{D}} \quad (5)$$

The bulk of hidden units have low correlation to the label. As shown in Figure 2E for randomly selected units, their distribution of inputs in the two classes overlap. However, number of units exhibit high correlation with the label (tail of distribution in 2D), separating well the two classes. Since the label information captured by the RBM

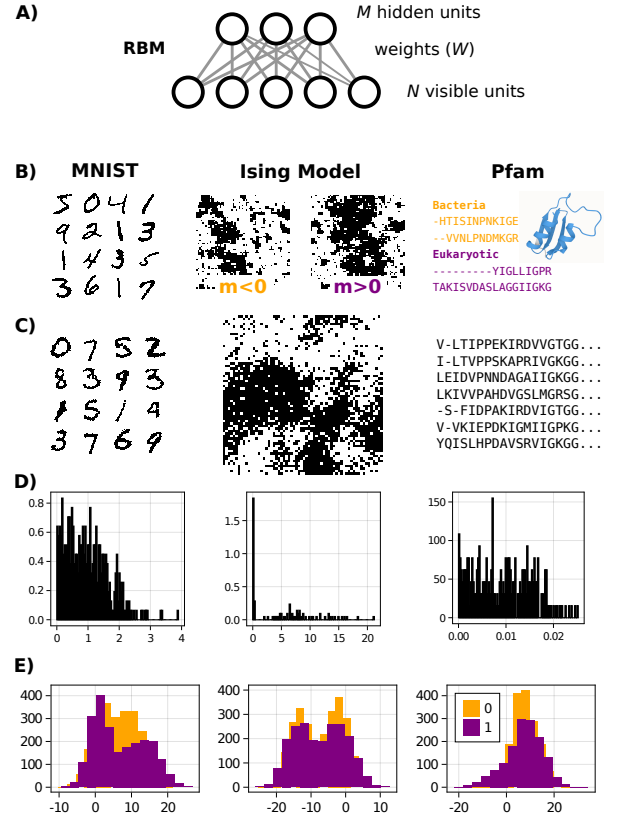


FIG. 2. **Datasets and entanglement of representations.** **A)** The standard RBM is a bipartite graphical model, consisting of a layer of N visible units v_i and a layer of M hidden units h_μ , which interact via an array of weights $w_{i\mu}$. **B)** Different datasets considered in the paper: the MNIST database of handwritten digits [22]; the two-dimensional Ising model; and multiple sequence alignments from the Pfam database [23], shown here for the PF00013 family example. **C)** RBM generated samples. **D)** Histogram of correlations between hidden unit inputs and the label. **E)** Input histograms of representative hidden units of RBMs trained on the three datasets, with colors matching the labels.

is distributed among these units, manipulating only the most correlated units is not sufficient to set the label of generated data (see Supplementary materials). The disadvantage of this representation is that to generate data of a desired class, the state of all these hidden units must be set in a concerted manner.

III. LEARNING OF DISENTANGLED REPRESENTATIONS

As seen above learning complex data with RBM generically results in a wide distribution of input-label correlations, extending over a large number of hidden units. Our strategy for disentangling and manipulating representations is to drastically alter this distribution by imposing adequate constraints on the interaction weights throughout the learning process.

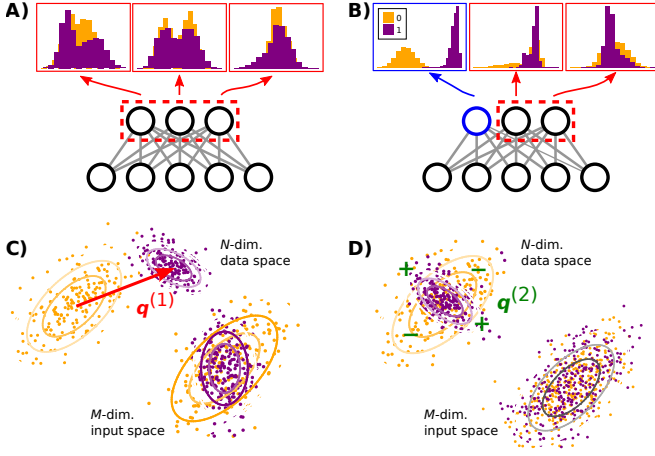


FIG. 3. **Model schema.** **A)** Constraints imposed on all hidden units, promote overlapping hidden input distributions of the two classes. **B)** Constraints imposed on a subset of hidden units (red), promotes class separation on the remaining hidden units (blue). **C)** First-order constraint (6) ensures that the classes have the same means in input space, by imposing orthogonality of the weights to the vector separating their centers of masses in data space (red). **D)** Second-order constraint (9) ensures that the two classes have the same covariance in input space.

Ideally constraints should impose that mutual information, rather than correlations, vanishes. Due to the difficulty in computing mutual information we focus on correlations, at different orders in the hidden inputs, as they offer a good compromise between computational efficiency and performance. Focusing on inputs I_μ rather than on latent variables h_μ follows a two-fold motivation. First, the constraints on the weights $w_{i\mu}$ resulting from the vanishing requirements on the correlations are simpler to interpret and to fulfill from a computational point of view. Second, given a data configuration \mathbf{v} , h_μ is a stochastic variable conditioned to I_μ ; by virtue of the data processing inequality [27] the mutual information between labels u and inputs I_μ upper bounds its counterpart between u and h_μ ; enforcing low mutual information between labels and inputs therefore immediately imply that latent variables are not informative about labels. Two goals can be pursued:

- A. *Approximating as best as possible the data distribution, while removing as much information as possible about their labels.* This can be achieved by an architecture in which all hidden units are under strong constraints, see Figure 3A.
- B. *Reproducing as best as possible the data distribution, while concentrating as much information as possible about their labels on one (or few) hidden units.* This can be achieved by an architecture in which a few hidden units are left unconstrained, while all the other ones are under strong constraints, see Figure 3B.

For the sake of simplicity we present the approach in the case of binary labels $u = 0, 1$ (equivalently, $u = \pm 1$). An extension to labels with more than two values is immediate, and will be discussed in the applications.

A. Fully constrained RBM

Following Goal A we demand that all hidden-unit inputs I_μ are uncorrelated with the labels u across the data. The corresponding architecture is sketched in Figure 3A. A RBM trained under these constraints is not expected to be generative, *i.e.* to produce visible configurations similar to the training data. However it learns an approximate data distribution, in which information about the label has been degraded.

1. Linear constraints

In its simplest formulation the approach only considers linear correlations in the inputs, *i.e.* C_μ in Eq. 5. Constraint $C_\mu = 0$ can be rewritten as

$$\sum_{i=1}^N q_i^{(1)} w_{i\mu} = 0, \quad (6)$$

with

$$q_i^{(1)} = \langle u(\mathbf{v}) v_i \rangle_{\mathcal{D}} - \langle u(\mathbf{v}) \rangle_{\mathcal{D}} \langle v_i \rangle_{\mathcal{D}}. \quad (7)$$

The N -dimensional vector $\mathbf{q}^{(1)}$ is parallel to the line joining the centers of mass of the clouds of data points associated to, respectively, $u = 0$ and $u = 1$, see Figure 3C. Imposing $C_\mu = 0$ for all $\mu = 1, \dots, M$ is thus equivalent to looking for the RBM maximizing the log-likelihood \mathcal{L} in Eq. 4 under the constraints that all M weight vectors \mathbf{w}_μ are orthogonal to $\mathbf{q}^{(1)}$; this can be easily done by projecting the gradient of \mathcal{L} onto the space orthogonal to $\mathbf{q}^{(1)}$ after each update of the weights (see SI for details). In other words, the RBM is blind to the direction \mathbf{q} separating the clouds and is modeling only the statistical features of the data in the $N - 1$ -dimensional space orthogonal to $\mathbf{q}^{(1)}$.

The consequences of $\mathbf{w}_\mu \perp \mathbf{q}^{(1)}$ can be phrased in an adversarial context. Imagine a linear discriminator is trying to predict the labels $u(\mathbf{v})$ of data configurations \mathbf{v} based on the M -dimensional sets of inputs $I_\mu(\mathbf{v})$. In practice a linear discriminator is parameterized by M weights a_μ , and assigns a probability $\pi(\sum_\mu a_\mu I_\mu(\mathbf{v}))$ to, say, label $u = 1$ (and probability $1 - \pi$ to $u = 0$) given \mathbf{v} , where π is some sigmoid function comprised between 0 and 1. The parameters a_μ are fitted to maximize the probability that the discriminator makes the correct prediction. In geometrical terms, this is equivalent to finding the hyperplane (orthogonal to \mathbf{a} in M dimensions) separating the classes of data points \mathbf{I} associated to $u = 0$ and to $u = 1$ with the largest margin [28]. We show in SI

that, under the conditions expressed in Eq. (6), the best linear discriminator cannot do better than random guessing of the labels. In other words, imposing constraints (6 is equivalent to demanding that no adversarial linear discriminator looking at hidden-unit inputs be able to predict the labels associated to configurations.

2. Quadratic constraints

Even if no linear discriminator can recover the label from the inputs I_μ , more complex machines, such as deep neural networks, could still be able to predict the label [29] if the mutual information between u and $\mathbf{I} = (I_1, I_2, \dots, I_M)$ is non-zero. Imposing $C_\mu = 0$ can be seen as a first-order approximation to the stronger condition that the mutual information between the label and the inputs vanishes, $\text{MI}(u, \mathbf{I}) = 0$. The latter implies that not only the linear correlations C_μ , but also all higher-order connected moments between u and \mathbf{I} vanish. In particular, the second-order correlations

$$C_{\mu,\nu} = \langle u(\mathbf{v}) I_\mu(\mathbf{v}) I_\nu(\mathbf{v}) \rangle_{\mathcal{D}} - \langle u(\mathbf{v}) \rangle_{\mathcal{D}} \langle I_\mu(\mathbf{v}) I_\nu(\mathbf{v}) \rangle_{\mathcal{D}} \quad (8)$$

should also vanish. Setting $C_{\mu,\nu} = 0$ for all pairs μ, ν in Eq. (8) forces the two classes of data attached to $u = 0$ and $u = 1$ to have identical covariance matrices in the input space. These constraints imply that no kernel-based adversarial discriminator, where the kernel is a quadratic function of the inputs, would be able to predict the label values (see SI for a proof). More generally, higher-order constraints would rule out the possibility for discriminator adversaries with polynomial kernels of higher degrees to successfully classify the data [30].

In practice, setting $C_{\mu,\nu} = 0$ amounts to imposing a quadratic constraint over the weight vectors:

$$\sum_{i,j=1}^N q_{i,j}^{(2)} w_{i\mu} w_{j\nu} = 0, \quad (9)$$

where the mean difference between the covariance matrices of the two classes of data is defined through

$$q_{i,j}^{(2)} = \langle u(\mathbf{v}) v_i v_j \rangle_{\mathcal{D}} - \langle u(\mathbf{v}) \rangle_{\mathcal{D}} \langle v_i v_j \rangle_{\mathcal{D}}, \quad (10)$$

see illustration in Figure 3D. To draw a physical analogy, the $\mathbf{q}^{(2)}$ matrix looks like the quadrupole tensor separating positive and negative charge distributions in electrostatics, while $\mathbf{q}^{(1)}$ is analogous to a dipole moment.

To implement constraints (9) in practice, we add the left-hand side of (9) squared to the optimization objective during learning times a large penalty term. See SI for details.

The matrix $\mathbf{q}^{(2)}$ defined in (10) is estimated on empirical data and is subject to sampling noise. In practice, from finite datasets one can extract reliable estimates only of the top components of $\mathbf{q}^{(2)}$, while the empirically observed lower components will be dominated by

noise. The Marchenko-Pastur (MP) law [31], describing the spectrum of correlation matrices in the null model case of independent variables can be used to estimate the thresholds between eigenvalues dominated by noise and eigenvalues reflecting the presence of structure in the data. MP spectrum predicts that all eigenvalues λ located in the range $[\lambda_-; \lambda_+]$ have to be discarded, with $\lambda_{\pm} = (1 \pm \sqrt{r})^2$, where $r = N/B$ is ratio of the numbers of variables and of samples. As an example, for the MNIST0/1 dataset, we estimate $\lambda_+ \simeq 1.6$ for both 0 and 1 digits. Out of the 784 eigenvalues of $\mathbf{q}^{(2)}$, only 60 (61) are larger than this bound for the 0's dataset (1's). The above discussion suggests replacing the full matrix $\mathbf{q}^{(2)}$ with a low-rank approximation focusing on the top components only. A lower-rank version of $\mathbf{q}^{(2)}$ also implies that the weights have more degrees of freedom, since (9) does not affect the weights components belonging to the kernel of $\mathbf{q}^{(2)}$. In practice, penalizing the squared norm of the left-hand side of (9) during training, automatically places more weight on constraints associated to the top components of $\mathbf{q}^{(2)}$, and neglects lower components.

B. Partially constrained RBM

We now consider Goal B. Our objective is to concentrate the information about the labels on one of few hidden units (hereafter referred to as "released"). For this purpose we consider the architecture of Figure 3B. The weights attached to these released hidden units are unconstrained during training, while the other weights are subject to linear or quadratic constraints in Eqs. (6) & (9), as in Goal A. Informally speaking, this strategy will condensate the distributed, weak correlations present across an extensive ($\propto N$) number of hidden units in standard RBM representations (Figure 2D) into extensive (growing with N) correlations present on an intensive number of released hidden units only.

1. Manipulation of label-determining hidden units

As a consequence, the values of the released hidden units strongly affect the conditional distribution of visible configurations, and act as knobs that can be manipulated to generate data with desired labels. Manipulation is carried out as follows; to lighten notations we assume that a single hidden unit, say, $\mu = 1$, is released. The value of this unit, h_1 , is fixed (to 0 or 1). We then sample the remaining hidden units (attached to the constrained weights) and the visible units using alternate Gibbs sampling (SI). The visible configurations \mathbf{v} are then distributed according to a conditional probability $P(\mathbf{v}|h_1)$, and span a class of the data corresponding to a specific label value u . Flipping h_1 to $1 - h_1$ allows us to change class.

2. Cost of disentanglement

Constraining all weight vectors (Goal A) is damaging the capability of RBM to reproduce the data distribution. The loss in performance is measured by the change in log-likelihoods of test data due to the partial erasure of information about the labels,

$$\Delta\mathcal{L}_{\text{part. erasure}} = \mathcal{L}_{\text{unconstr.}} - \mathcal{L}_{\text{constr.}}. \quad (11)$$

In the equation above, $\mathcal{L}_{\text{constr.}}$ denotes the log-likelihood of data estimated with the fully-constrained RBM, and $\mathcal{L}_{\text{unconstr.}}$ corresponds to the standard (unconstrained) RBM. As we shall see in subsequent applications this difference is generally large.

Once one or few hidden units are released (Goal B), the test log-likelihood increases to $\mathcal{L}_{\text{rel.}}$. We define the cost for disentangling representations through

$$\Delta\mathcal{L}_{\text{disent.}} = \mathcal{L}_{\text{unconstr.}} - \mathcal{L}_{\text{rel.}}. \quad (12)$$

This cost is guaranteed to be non-negative if both RBM are trained with equal hyperparameters, e.g. have the same number of hidden units and weight regularizations.

IV. APPLICATION TO MNIST HANDWRITTEN DIGIT IMAGES

We illustrate our approach on the MNIST handwritten digit dataset [22]. Pixel intensities are binarized through thresholding at 0.5. For simplicity, we start by considering the subset of images containing only digits 0 and 1 (MNIST0/1), for which the class label u is binary. Similar analysis on other pairs of digits are reported in SI.

A. Learning with standard RBM

We start by training a standard RBM on MNIST0/1, with $M = 400$ binary hidden units and $N = 28 \times 28$ visible units, through maximization of the log-likelihood (4). Figure 4A shows Markov chains of samples derived from Gibbs sampling of the resulting models. The machine generates strings of 0's or 1's, depending on the initial condition, with very rare transitions between these classes. Note that the absence of transitions from 0 to 1 (or vice versa) is likely due to the strong dissimilarities between these two digits in configuration space and the lack of low energy configurations connecting them; training the RBM on all digits tends to connect these two modes and to increase the frequency of observed transitions.

To quantify the information content in the inputs about the labels (digit value) we need to estimate the mutual information $\text{MI}(u, \mathbf{I}(\mathbf{v}))$. While computing MI is very hard, a tractable lower bound can be obtained

through the Gibbs variational inequality, [27]

$$\begin{aligned} \text{MI}(u, \mathbf{I}(\mathbf{v})) &\geq \sum_{u, \mathbf{v}} P_{\mathcal{D}}(u, \mathbf{v}) \ln \left(\frac{P_{\text{class}}(u | \mathbf{I}(\mathbf{v}))}{P_{\mathcal{D}}(u)} \right) \\ &= \mathcal{S}_{\text{label}} + \mathcal{L}_{\text{class}} \end{aligned} \quad (13)$$

where $P_{\mathcal{D}}(u, \mathbf{v})$ is the empirical distribution of labeled data, and $P_{\text{class}}(u | \mathbf{I}(\mathbf{v}))$ is any conditional distribution, implemented here by a classifier attempting to predict the label. By rearranging terms, this equals the entropy of labels in the data ($\mathcal{S}_{\text{label}}$) plus the log-likelihood of the classifier averaged over held out data ($\mathcal{L}_{\text{class}}$).

This lower bound to MI is shown in Figure 4B (black bars) for classifiers of increasing complexity, corresponding to two-layer networks with a hidden layer of increasing width (horizontal axis in the figure), see SI for details about the architecture and training of these classifiers. The simplest network is a linear classifier (perceptron, width = 0), and already achieves nearly perfect prediction accuracy (SI). In addition the weights of this optimal linear classifier are distributed over all hidden units, showing that information about the label is distributed across the latent representation. As the width of the classifier increases the lower bound to MI saturates at a value close to 1 bit, the maximum possible for two label classes, indicating that the RBM inputs capture maximum label information. We emphasize that the RBM has no direct access to the label values during training.

B. Partial erasure of information with fully constrained RBM

We next train RBM with constrained applying on the weight vectors attached to all hidden units.

1. Linear constraints

Figure 4A (bottom, red) shows typical configurations generated by RBM trained with Eq. (6). As expected these configurations tend to be blurred mixtures of 0's and 1's.

A simple linear discriminator looking at the inputs to the hidden units is unable to predict the labels of these digits, in agreement with the adversarial interpretation of Eq. (6). However, information about the digit class is still present in the RBM representations through higher-order correlations. Sufficiently complex classifiers are able to recover the label of data digits with maximum accuracy (Figure 4B), and give lower bounds to MI close to unity. This result shows that, while condition (6) is not sufficient to erase the label information from the representation extracted by the RBM, it does make retrieval of this information more difficult.

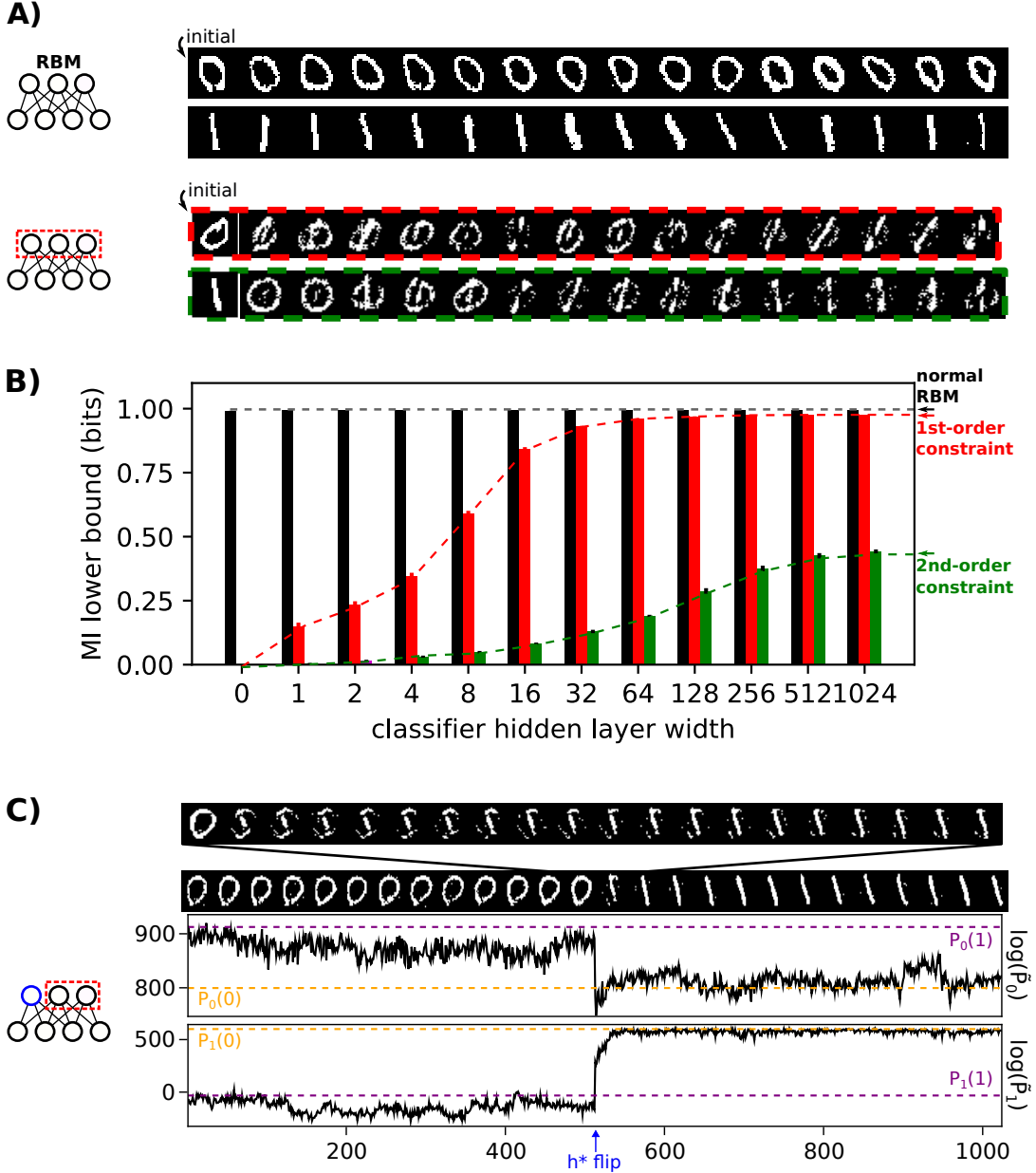


FIG. 4. **Manipulating representations of RBM trained on MNIST0/1.** **A)** Samples generated by RBM initialized with a data image (0 or 1). Top two rows: standard (unconstrained) RBM; Bottom two rows show samples from RBM trained with linear (red dashed) and quadratic (green dashed) constraints. In both cases, a Markov chain was generated by Gibbs sampling (starting from a 0 or a 1 data digit), and images were saved every 64 steps, until reaching a total of 16 samples as shown. **B)** Lower bound $S_{\text{label}} + \mathcal{L}_{\text{class}}$ to the mutual information between inputs and labels, see Eq. (13), vs. classifier width. The bounds to MI is measured in bits and shown in discontinuous lines. Colors correspond to the different RBM models. Black: standard/unconstrained; Red: fully constrained with linear constraints, see Eq. (6)); Green: fully constrained with quadratic constraints, see Eq. (9). **C)** Samples from RBM trained with 1st-order constraint acting on all but one hidden unit, which is flipped at the middle of the MC chain (blue arrow). Starting from a 0 data digit, samples were saved every 64 Gibbs steps. Top panel shows a zoomed view of the transition, with images every 3 steps instead. The lower panels show the logarithm of the unnormalized probability, $\ln \tilde{P}(\mathbf{v}) = \ln \left(\sum_{\mathbf{h}} e^{-E(\mathbf{v}, \mathbf{h})} \right)$ of generated digits by constrained RBMs, evaluated on RBMs trained only on 0s (RBM0) or 1s (RBM1). Purple and orange dashed lines correspond to the average $\ln \tilde{P}(\mathbf{v})$ of data digits 0 and 1.

2. Quadratic constraints

Imposing the stronger, quadratic constraints in Eq. (9) results in worse quality samples, see green row in Figure 4A, bottom. Figure 4B shows that simple classifiers trained are unable to predict the labels from the inputs. Interestingly, more complex classifiers achieve a moderate non-zero prediction accuracy, but provide substantially lower estimates of the mutual information than when trained on linearly-constrained RBMs (compare green and red bars). The lower bounds to MI seems to saturate to a value well below 1 as the classifier widths increase. These results indicate that quadratic constraints erase a sizable part of the information about the labels.

C. Manipulating representations and digits with partially constrained RBM

We now impose linear constraints (6) to all but one (blue) hidden units. As stated in Goal B, our intention is to promote concentration of label information on this released unit, see Figure 3B. After learning the released weight vector is similar (up to a global scale factor) to vector $\mathbf{q}^{(1)}$, see SI, a direction forbidden to the other hidden units. Hence the average value of the unit conditioned to a visible configuration (digit) is an excellent predictor of the corresponding label.

Samples generated by the RBM are nice-looking 0s or 1s, in a manner consistent with the state of the released hidden unit. Furthermore, manipulating the state of this hidden unit i.e. freezing it to 0 or 1 helps generating samples with desired labels. We show in Figure 4D numerical experiments illustrating the effects of such manipulations. We initialize the RBM with a digit (0 in Figure 4D) extracted from the MNIST0/1 data set, and samples new configurations through alternate Gibbs samplings. As with standard RBM the samples vary over time, but the digit class remain unchanged. We then flip the state of the hidden unit (middle of Figure 4D). As a consequence, the resulting visible configuration converges to the other digit class, after some short transient (see top part of panel).

To evaluate the quality of the generated digits, we train two RBMs only on 0s or 1s, respectively, and evaluate the log-likelihoods of the generated digits on two standard RBMs, one trained with 0 digits only, and another trained on 1's only. These two machines provide expected reference scores for 0's and 1's. Figure 4E show that the generated digits are of good quality, with log-likelihood values comparable to the ones of the data.

D. Case of more than two digits

While we have focused on the case of binary labels so far, our approach can be easily adapted to more than two classes. We consider the case of D classes, and use

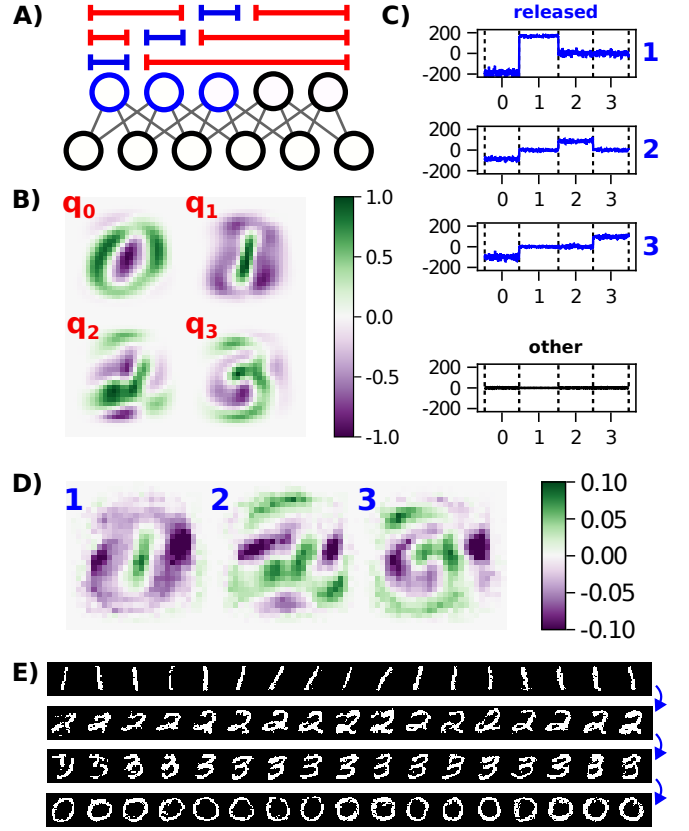


FIG. 5. **Manipulating representations of RBM trained on MNIST0/1/2/3.** **A)** Sketch of the constraints applied to hidden unit weights in the case of multiple classes, here, $D = 4$. **B)** Vectors $\mathbf{q}_d^{(1)}$ for digit classes 0, 1, 2 and 3, see Eq. (14). **C)** Inputs received by the released (in blue) hidden units, when data digits 0, 1, 2 or 3 are presented, in order as indicated on the x -axis. In the bottom panel, inputs received by a random hidden unit from the constrained group (black) is shown. **D)** Weights $w_{i\mu}$ learned weights by the released hidden units $\mu = 1, 2, 3$. **E)** Samples generated from this machine by Gibbs sampling (images shown are taken every 64 steps). First (top row), released unit 1 is active, while the other two are inactive. Then, we activate unit 2 (second row) while inactivating unit 1 (blue arrow), and similarly for 3 (third row). In the last row, all three units are inactive.

one-hot encoding for the labels, i.e. introduce D labels u_d , one for each class $d = 0, 1, \dots, D - 1$. Due to one-hot encoding prescription each data configuration \mathbf{v} is such that $D - 1$ labels $u_d(\mathbf{v})$ vanish and one is equal to 1.

Analogously to (6), we define D vectors (in the N -dimensional space of data)

$$\mathbf{q}_d^{(1)} = \langle u_d(\mathbf{v}) \mathbf{v} \rangle_{\mathcal{D}} - \langle u_d(\mathbf{v}) \rangle_{\mathcal{D}} \langle \mathbf{v} \rangle_{\mathcal{D}}. \quad (14)$$

We then generalize Eq. (6) to multiple classes by imposing that weight vectors be orthogonal to all $\mathbf{q}_d^{(1)}$, with $d = 1, \dots, D$. It is easy to check that the D vectors in Eq. (14) sum up to zero, a consequence of the one-hot encoding scheme. We therefore consider only the last $D - 1$ vectors, with indices $d = 1, 2, \dots, D - 1$ to obtain

linearly independent constraints acting on the weights.

In practice the constraints $\mathbf{w}^\mu \perp \mathbf{q}_d^{(1)}$ are enforced through the architecture shown in Figure 5A, in which a set of $D - 1$ hidden units are released with respect to a *single* $\mathbf{q}_d^{(1)}$ and constrained to be orthogonal to all the other vectors. In this way, when activating one of this hidden units, say, μ , the corresponding digit $d = \mu$, is expected to be sampled on the visible layer. When all first $D - 1$ hidden units are silent, digit $d = 0$ is expected to be sampled.

We illustrate this approach in the case of $D = 4$ digits, with RBMs trained from MNIST0/1/2/3. The vectors $\mathbf{q}_d^{(1)}$ in Eq. (14) are shown in Figure 5B. After training the RBM under the orthogonality constraints, the released hidden units $\mu = 1, 2, 3$ are strongly activated by, respectively, digits $d = 1, 2, 3$. In Figure 4C we show the average inputs to these hidden units when data digits are presented on the visible layer of the RBM; the corresponding weight vectors are depicted in 5D. When digit 0 is present on the visible layer, the three hidden units are silent. Other hidden units are weakly activated by the different digits and capture information (small stretches, local contrast) crucial for generating high-quality digits but not directly related to their identity, see panel “other” in 5C.

We next manipulate these units to generate digits out of one of the four classes. The outcome is shown in Figure 5E, where the Markov chain is initialized with a 1 digit from the MNIST data, and the first released hidden unit ($\mu = 1$) is on, while the other two ($\mu = 2, 3$) are off. Sampling the RBM in this condition generates a string of 1’s as illustrated in the figure. Turning this unit off and turning the second $\mu = 2$ on now produces a transition in the visible layer, and generates digits 2. Iterating this procedure, we generate 3’s, and finally 0’s by turning off all released hidden units (last row in Figure 5E).

V. APPLICATION TO THE TWO-DIMENSIONAL ISING MODEL

The two-dimensional Ising model is defined by the following energy function over $N = L^2$ spin configurations $\mathbf{v} = (v_1, v_2, \dots, v_N)$,

$$E(\mathbf{v}) = - \sum_{(i,j)} v_i v_j \quad (15)$$

where the sum runs over pairs (i, j) of nearest neighbours on a two-dimensional squared grid with $L \times L$ sites. Each spin v_i can take ± 1 values. We choose periodic boundary conditions, that is, site $(1, 1)$ is interacting with sites $(1, 2)$, $(2, 1)$, $(L, 1)$ and $(1, L)$. The model assigns probabilities given by the Boltzmann law $P_{\text{Ising}}(\mathbf{v}) \propto e^{-\beta E(\mathbf{v})}$ to configurations \mathbf{v} , where β is the inverse temperature; we hereafter denote the average over P by $\langle \cdot \rangle$. In the infinite L limit, the model undergoes a phase transition

from a paramagnetic phase ($\beta < \beta_c$) in which the magnetization

$$m = \left\langle \left| \frac{1}{N} \sum_i v_i \right| \right\rangle \quad (16)$$

vanishes to a ferromagnetic phase ($\beta > \beta_c$), in which $m > 0$ [24]. The transition occurs at a critical inverse temperature $\beta_c \approx 0.44$, computed exactly by L. Onsager [32], see Figure 6.

A. Sampling the Ising model at equilibrium

We start by generating up to 10^6 samples from the Ising model through Monte Carlo (MC) simulations, at different inverse temperatures in the range $0.35 \leq \beta \leq 0.5$. To quickly equilibrate at all temperatures the MC chain includes both local Metropolis updates and global Wolff cluster moves, known to be efficient to sample the model near β_c [33]; Details about the implementation can be found in SI. The magnetization M and the heat capacity

$$C = \frac{\beta^2}{N} (\langle E^2 \rangle - \langle E \rangle^2) \quad (17)$$

are shown as functions of the inverse temperature in Figure 6A for two system sizes, $L = 32$ and $L = 64$. Additional observables, such as the susceptibility

$$\chi = \frac{\beta}{N} \left[\left\langle \left(\sum_i v_i \right)^2 \right\rangle - \left\langle \sum_i v_i \right\rangle^2 \right] \quad (18)$$

and the correlation length are reported in SI. A peak in the heat capacity (and in the susceptibility) signals the cross-over between the two phases, when β gets close to β_c , with a shift that vanishes with increasing L as predicted by finite size-effects theory.

B. Learning with standard RBM

We then use the MC samples as training data for an unconstrained RBM, with visible units taking ± 1 values. To enforce the global sign symmetry of the energy, i.e. $E(-\mathbf{v}) = E(\mathbf{v})$, see Eq. (15), we choose hidden units $h_\mu = \pm 1$ (instead of 0,1 as in the MNIST case) and vanishing biases on the both visible ($g_i = 0$) and hidden ($\theta_\mu = 0$) units. The training phase thus consists in inferring the RBM weights $w_{i\mu}$ only.

We check that the log-likelihood $\log P(\mathbf{v})$ of test MC data estimated with the trained RBM correlate with the Ising energy $E(\mathbf{v})$ (SI). The weights learned by the RBM exhibit localization patterns (see Figure 6G) at low temperatures, in agreement with observations reported in previous works on 1-D Ising model [26].

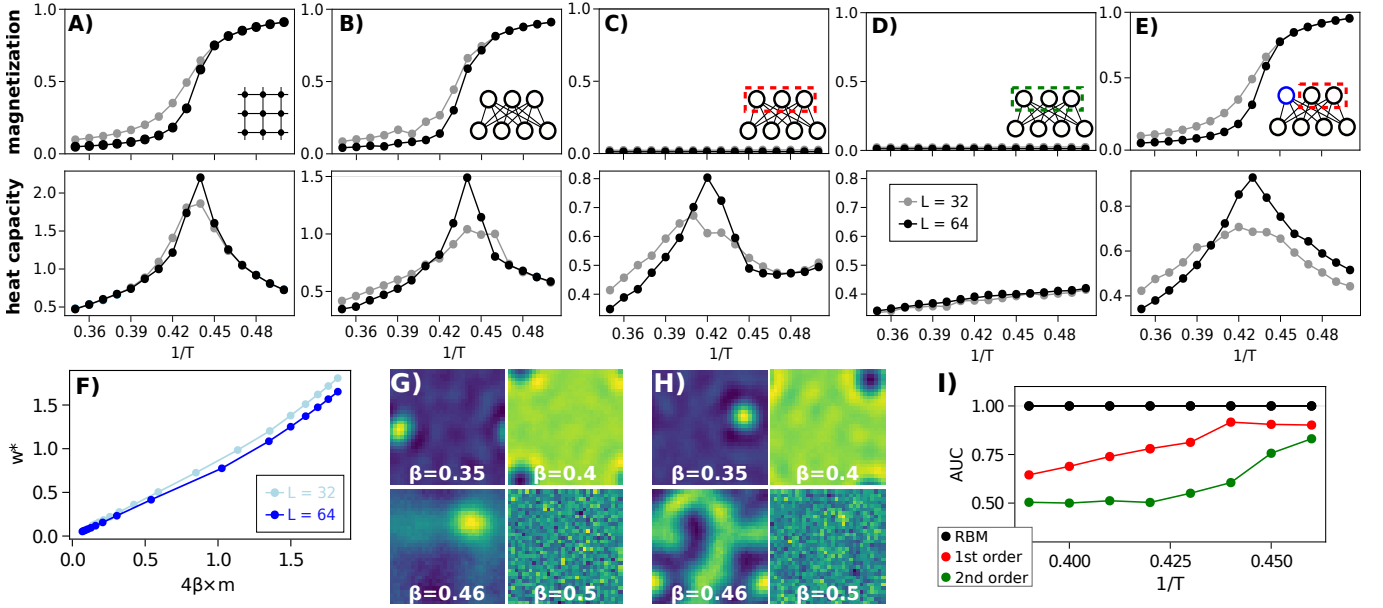


FIG. 6. **Learning RBMs on two-dimensional Ising model data.** **A)** Magnetization and heat capacity as functions of temperature for the samples generated by the Ising model (15). **B)** Magnetization and heat capacity of samples generated by an RBM trained on the Ising data. **C)** Magnetization and heat capacity of samples generated by RBM with constraint (6) acting on all hidden units. **D)** Magnetization and heat capacity of samples generated by RBM with quadratic constraint (9) acting on all hidden units. **E)** Magnetization and heat capacity of samples generated by RBM with linear constraint (6) acting on all but one hidden unit. **F)** Free weights attached to the released hidden unit compared to 4β times the magnetization of the Ising model. **G,H)** Typical weights learned by the RBM at selected temperatures ($1/T = 0.35, 0.4, 0.46, 0.5$), for the unconstrained RBM, and for the RBM with the 1st-order constraint. **I)** Maximum AUC of classifiers trained to predict the sign of the sample magnetization from the RBM inputs.

We generate samples from these RBMs learnt at different β 's using alternate Gibbs sampling, and evaluate the magnetization, heat capacity, and susceptibility. Results are in agreement with the same quantities computed from samples of the Ising model distribution, see Figure 6B. This observation is consistent with literature [25, 34, 35], where RBMs were shown to be able to accurately fit statistical physics models such as the Ising model.

C. Partial erasure of information with fully constrained RBM

We hereafter choose that the label $u = \pm 1$ associated to a configuration of spins \mathbf{v} is the sign of its magnetization,

$$u(\mathbf{v}) = \text{sign} \left(\sum_i v_i \right). \quad (19)$$

1. Linear constraints

By symmetry, the vector $\mathbf{q}^{(1)}$ in Eq. (6) has uniform components $q_i^{(1)} = q^{(1)}$ due to the translation invariance of the lattice resulting from periodic boundary conditions. Imposing the linear constraint in Eq. (6) thus

amounts to demanding that all weight vectors sum up to zero, i.e. $\sum_i w_{i\mu} = 0$ for $\mu = 1, \dots, M$.

We then train a RBM on the MC data under these constraints. The log-likelihoods of test Ising configurations are poorly correlated with the Ising model energies in Eq. (15), see SI. In addition, RBM generated samples show no magnetization at any inverse temperature, even for $\beta > \beta_c$, see Figure 6C. Surprisingly, however, other observables such as heat capacity (Figure 6C) or the susceptibility (SI) exhibit a peak at the cross-over inverse temperature. We conclude that, due to the linear constraint on the weights, the RBM is unable to express non-zero first moment for the spins, but a substantial part of higher-order correlations between spins is still correctly captured and reproduced. We will come back on the interpretation of the effective energy corresponding to this fully-constrained RBM in Section V E.

2. Quadratic constraints

We next apply second-order constraints (9) to all weight vectors of the RBM. Due to the global invariance of the Ising energy under spin reversal $\mathbf{q}^{(2)} = 0$ abiding to definition (10). However, the reversal symmetry is lifted in the presence of an arbitrary small uniform external field Δ , i.e. $E(\mathbf{v}) \rightarrow E(\mathbf{v}) - \Delta \sum_i v_i$. We show in SI

that, to first order in Δ , $\mathbf{q}^{(2)} \simeq \frac{1}{2} \Delta \mathbf{Q}^{(2)}$ with

$$Q_{i,j}^{(2)} = \left\langle \left| \sum_k v_k \right| v_i v_j \right\rangle_{\mathcal{D}} - \left\langle \left| \sum_k v_k \right| \right\rangle_{\mathcal{D}} \langle v_i v_j \rangle_{\mathcal{D}}. \quad (20)$$

The tensor $\mathbf{Q}^{(2)}$ can be estimated numerically, and used to constrain the weight vectors through Eq. (9).

RBM learnt under these quadratic constraints generate spin configurations with zero magnetization, as in the case of linear constraints, see Figure 6E. Remarkably, the specific heat and the susceptibility show no peak as β is varied, suggesting that quadratic constraints on the weights have much stronger impact on the distribution of spin configurations. The heat capacity in particular, has a mild monotonic increasing tendency with β , attaining similar values to the original model at low and high temperatures.

However, inference of the magnetization sign is still possible from the hidden representation, although with degraded performance. For each inverse temperature, we trained classifiers of varying complexity, and measured their performance in predicting the labels. The resulting AUC are shown in Figure 6I, and are above chance level (.5) at high β . This indicates that higher-order correlations presumably present in the inputs of full-constrained RBM (such as the Binder cumulant [36]) can be used for predicting labels with some success, a situation reminiscent of the partial erasure of information we find in the MNIST0/1 case (Figure 4B).

D. Manipulating representations and spin configurations with partially constrained RBM

We now apply constraint (6) on all but one hidden unit when training the RBM on the Ising data. The released hidden unit learns a weight vector which is approximately proportional to $\mathbf{q}^{(1)}$, that is, the weights connecting to this unit are uniform over the visible layer, with a common value hereafter referred to as w^* . The resulting RBM then has one hidden unit that controls the sign of the magnetization of the generated samples, while the remaining hidden units capture local correlated patterns of neighboring spins. Indeed, the constrained weights display localized patterns similar to those of unconstrained RBM (Figure 6E). In addition, the RBM reproduces the behavior of all observables as the inverse temperature is varied (Figures 6E and SI). These results strongly suggest that the constraints (on all but one) weight vectors applied during learning do not impair the ability to fit the data, but only serve to reorganize the latent representations. In addition to (6), we can also impose constraints (9) on all but one hidden units, with similar results as those reported (not shown).

E. Effective energy resulting from constraints

A heuristic argument allows us to better understand the nature of the distribution expressed by the fully-constrained RBM (linear case), in particular, why generated configurations have zero magnetization while encoding non-trivial spin-spin correlations (Figure 6C).

Let us first notice that the general expression for the log-probability of a visible configuration \mathbf{v} in the RBM reads, due to the absence of biases on the units,

$$\log P_{\text{RBM}}(\mathbf{v}) = \sum_{\mu=1}^M \log \cosh \left(\sum_i w_{i\mu} v_i \right), \quad (21)$$

up to an irrelevant additive constant. This formula applies in particular to the released RBM of Section V D, in which all but one hidden unit, say, $\mu = 1$, are constrained to satisfy Eq. (6). Based on our previous finding that $w_{i,1} \simeq w^*$, we obtain

$$\log P_{\text{rel.}}(\mathbf{v}) \simeq \sum_{\mu=2}^M \log \cosh \left(\sum_i w_{i\mu} v_i \right) + w^* \left| \sum_i v_i \right|, \quad (22)$$

where we have approximated $\log \cosh x \simeq |x|$ for large arguments x and have again neglected additive constants. Based on Eq. (22) we may proceed in two steps. First, as we empirically find that the released RBM is a good approximation of the ground-truth Ising distribution, we approximate $\log P_{\text{rel.}}$ with $\log P_{\text{Ising}}$. Second, the first term on the right-hand side of Eq. (22) expresses the log-probability of \mathbf{v} computed by a RBM with weight vectors constrained to be orthogonal to $\mathbf{q}^{(1)}$, and can thus be identified with $\log P_{\text{constr.}}$. We conclude, using Eq. (15), that the effective energy function on the spin configuration encoded by the fully constrained RBM is approximately equal to

$$E_{\text{constr.}}(\mathbf{v}) \simeq - \sum_{(ij)} v_i v_j + \frac{w^*}{\beta} \left| \sum_i v_i \right|. \quad (23)$$

The effects of the constraints on the weights is to introduce a L_1 -like penalty against magnetized configurations opposing the Ising energy, which tends to align spins. This explains both the disappearance of magnetization and the remanent correlations observed in Figure 6C.

We can also estimate the value of w^* selected through learning of the fully-constrained RBM, with an heuristic argument. Consider a typical configuration of the Ising model at low temperature, i.e. in the ferromagnetic regime corresponding to magnetization $m^* \neq 0$. The effective field acting on spin, say, i , reads, according to Eq. (23),

$$g_i^{\text{eff}} = \sum_{j \in \mathcal{N}_i} v_j - \frac{w^*}{\beta} \text{sign}(m^*), \quad (24)$$

where \mathcal{N}_i refers to the neighbourhood of spin i on the squared grid. Taking the average over the spin i we obtain the mean value of the effective field

$$\langle g^{\text{eff}} \rangle = z m^* - \frac{w^*}{\beta} \text{sign}(m^*) , \quad (25)$$

where $z = 4$ is the coordination number on the grid. We conclude that the effective field vanishes when

$$w^* = \beta z |m^*| . \quad (26)$$

The above expression gives the minimal strength of the L_1 penalty capable of counterbalancing the local interactions tending to magnetize spins. It is expected to vanish in the paramagnetic regime. Higher values are disfavored during the RBM training phase as they would assign higher energies $E_{\text{constr.}}$ in Eq. (23) to typical magnetized Ising configurations, and thus lower likelihoods.

We compare the heuristic estimate for w^* provided by Eq. (26) to the numerical results for w^* obtained from training partially-constrained RBM on 2D-Ising data in Figure 6F. Despite the presence of finite-size effects, we observe a good agreement between Eq. (26) and the simulation results.

VI. APPLICATION TO PROTEIN SEQUENCES WITH TAXONOMY ANNOTATIONS

A protein family is a group of proteins that share a common evolutionary origin, reflected by their related functions and similarities in sequence or structure [23]. Protein families are often arranged into hierarchies, with proteins that share a common ancestor subdivided into smaller, more closely related groups. In recent years, RBMs have been successfully applied to extract structural, functional, and evolutionary information from the sequences attached to a protein family [18, 19, 37]. Our aim here is to use partially constrained RBM to disentangle the label defining the taxonomic domain (eukaryota or bacteria) a protein sequence belong to, and manipulate the domain-determining hidden unit to drive a continuous transition, or morphing, between one taxonomic domain to the other during sampling of artificial sequences.

A. The K homology domain

To illustrate the application of our model, we selected the K homology (KH) module, a common nucleic acid binding motif in proteins found in multiple species, both eukaryotic and prokaryotic. Structurally, KH domains adopt a globular fold, constituted by three alpha-helices and three beta sheets [39–41], as shown in Fig. 7A. A central feature of the KH domain is the presence of a signature IsoGlyXXGly motif (see Figure 7A & B), conserved across the entire family, which in cooperation with flanking helices, forms a cleft where recognition of four nucleotides in single-stranded DNA or RNA chains occurs

[41]. Mutations in these highly conserved residues result in loss of function [42]. In particular, substitution of the moderately conserved isoleucine following the Gly–Gly loop (two sites after) by Asn, in a KH domain locus of the fragile X mental retardation gene in humans, causes fragile X syndrome, a leading heritable cause of mental retardation [43].

We have selected this family in our work as it has a sufficient number of eukaryotic and bacterial sequences available in the PFAM database [23]. The PF00013 family of homologous sequences, includes $\sim 11,000$ bacterial sequences and $\sim 38,000$ eukaryotic sequences of the KH domain. After aligning, removing insertions and retaining only columns with less than 50% gap (deletions) content sequences end up having a common length of $L = 62$ amino acids. As the taxonomic origin of every sequence can be simply queried through the Uniprot database [44], we define label $u = 0$ and 1 for, respectively, bacterial and eukaryotic proteins. To reduce common ancestry bias, sequences are weighted according to their dissimilarity to other members of the same family [45, 46]: the weight assigned to a sequence is proportional to the inverse of the number of sequences in the family with a Hamming distance smaller than 20% of the sequence length. We also balance the total weights of eukaryotic and bacterial classes, so that both classes have equal weights.

Figure 7A shows the sequence logos of the eukaryotic (top) and bacterial (bottom) sequences in the family after carrying out the above pre-processing steps. Some features are shared across KH domain sequences in both sub-families, such as the well-conserved Gly–Gly loop (Figure 7B). Bacterial sequences have an overall larger content of gaps (deletions) with respect to the consensus alignment, reflecting sequence length differences in the two sub-families.

B. Learning a generative model with standard RBM

Multiple Sequence alignments are represented using categorical or Potts variables, each site of the alignment having one of 21 possible values (20 amino-acids and one gap value). Gaps are necessary to model sequences of varying lengths [45]. Using the one-hot-encoding a configuration \mathbf{v} of the visible layer encodes a sequence over $21 \times L$ units, where L is the sequence length.

We first train a RBM on the full alignment, containing both eukaryotic and bacterial sequences, following [18]. The RBM captures statistics of the sequence alignment, such as conservation profiles at each site. In addition, simple linear classifiers trained on top of the hidden layer of the RBM achieve AUCs of 0.9 in distinguishing between these two classes.

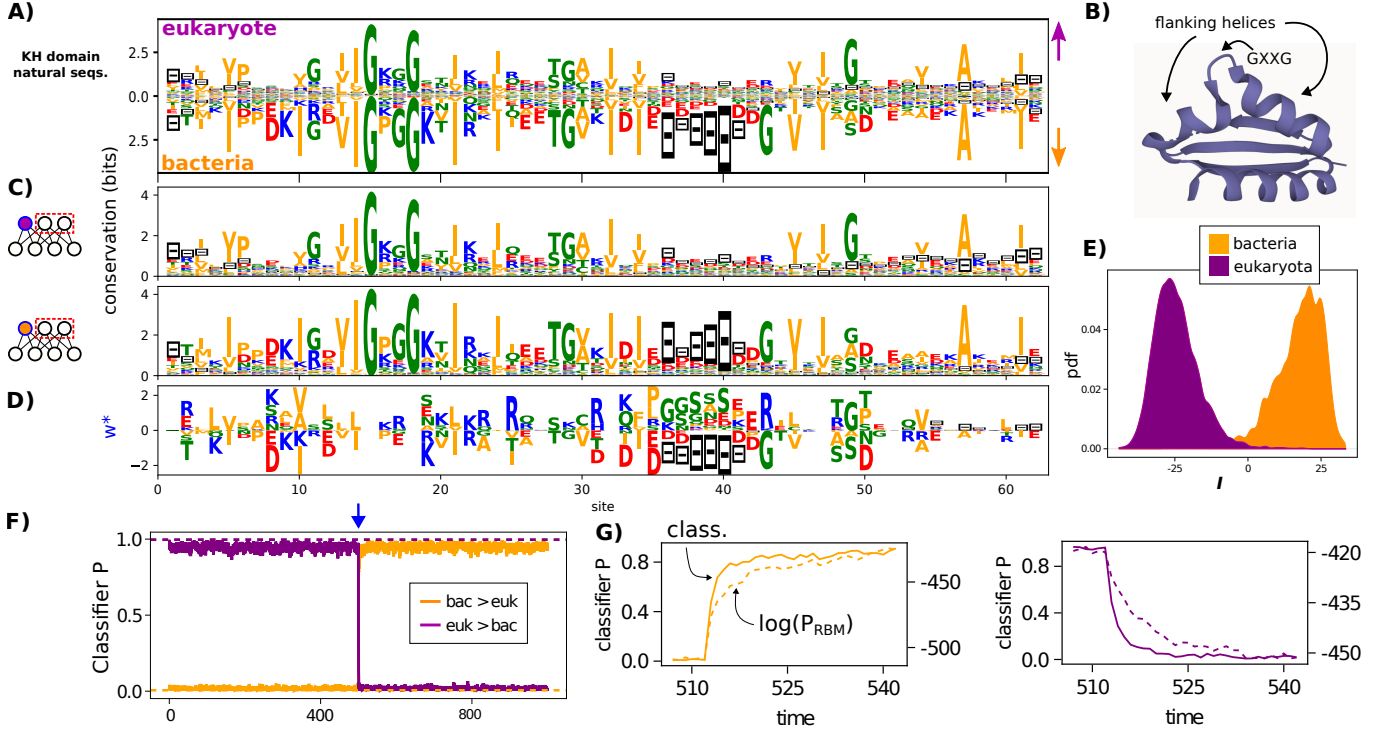


FIG. 7. **Taxonomy of protein families** **A)** Sequence logos of eukaryotic (purple, above) and bacterial (orange, below) sequences from the PF00013 protein family. We use the following color code: green for polar residues, blue for basic, red for acidic, and orange for hydrophobic. Gaps are shown in black. **B)** Ribbon structure of KH domain, showing locations of Gly–Gly loop and flanking helices. Image prepared with Mol* Viewer [38]. **C)** Sequence logos of 10,000 generated sequences, when the released hidden unit is set to 1 (top) or 0 (below). To ensure that sampling is equilibrated, we track the average and standard deviation of the energy of the samples in time, and saw that these statistics were essentially constant after ~ 200 steps (SI), suggesting that samples can be collected every 5,000 steps. **D)** Weights of the released hidden unit. **E)** Inputs received by the released hidden unit when presented with sequences from the two classes. **F)** Markov chain, started from bacterial (orange) or eukaryotic (purple) sequences from the data. The panel shows the probability of being eukaryotic vs. bacterial sequence in a perceptron classifier. Discontinuous lines are the average value for data sequences of each class. A total of 1024 Gibbs sampling steps were taken, and the flip of h_1 occurs at step 512 (blue arrow). **G)** Zoomed view near the transition, showing also the log of the unnormalized marginal $\log \tilde{P}_{\text{RBM}}(\mathbf{v})$ of sampled sequences (right axis), evaluated on an RBM trained on the full family.

C. Changing taxonomic domain with protein design

We then apply the linear orthogonality constraint in Eq. (6) to all but one weight vectors. The weights of the released hidden unit after training are shown in Figure 7D, and capture features that differentiate the two classes. For example, bacterial sequences tend to have deletions (gaps) around positions 35 - 40 of the alignment, indicating that this segment is often absent in bacterial sequences. The learned w_i^* reflect this by assigning negative weights to the gap symbol in this region. As a consequence, the distribution of inputs subtended by eukaryotic and bacterial sequences is well separated on this unit (Figure 7E). Conversely, features shared by eukaryotes and bacteria, such as the Gly–Gly loop, or the conserved I22, are ignored by \mathbf{w}^* .

We generate many samples from the RBM distribution, each conditioned to a fixed state of h_1 , corresponding either to bacterial ($h_1 = 0$) or eukaryotic ($h_1 = 1$) classes.

The sequence logos of the two sets of generated sequences are shown in Figure 7C; they closely match the ones of training data. The list of differences between the logos associated to the two sequence domains include:

1. The Gly–Gly loop is followed by a conserved Lys19 predominantly in bacteria, but not so in eukaryotic sequences.
2. Bacterial sequences conserve a Asp-Lys-Iso motif (positions 8-10) which the RBM with $h_1 = 0$ correctly emits, but not so in the $h_1 = 1$ case.
3. Besides the two Gly conserved in the entire family, eukaryotic sequences also conserve Gly49, a site which appears less conserved in bacteria which admit also Ala or Ser at this position. The RBM correctly observes these variations.
4. Iso10 is highly conserved in bacteria, while in eukaryotes this site is not conserved, admitting in particular Val, Ala.

These examples suggest that the RBM can sample each sub-family, conditioned on the value of h_1 .

Next, we sample the RBM starting from one bacterial or one eukaryotic sequence in the dataset as initial condition, and with h_1 set to the value matching the initial condition. After some steps, the value of h_1 is flipped, and we monitor the dynamical evolution of the generated samples. Figure 7F shows the probability that generated sequences are eukaryotic or bacterial, according to a linear classifier achieving AUC > 0.9 on held-out test data (see SI).

Figure 7G shows a magnified view of the classifier probabilities and of the log-likelihood in the vicinity of the hidden-unit switch. We evaluate the log-likelihood of the samples with a RBM trained on the full family (denoted $\log \tilde{P}_{\text{RBM}}$ in the figure). The class switch, as measured by the classifier score, occurs faster than the relaxation dynamics following the h_1 flip, as measured by the likelihood. This suggests that the sampled sequences retain other features unrelated to the labeled class, that relax at a slower rate.

VII. ESTIMATING THE COSTS OF PARTIAL ERASURE AND DISENTANGLEMENT

As discussed in III B 2, concentrating label information on few hidden units of the RBM, generally hinders the ability of the model to fit the data accurately, and results in a lower likelihood of test data. In this section we estimate the cost associated to disentanglement, focusing on the impact of linear constraints on the weights, see Eq. (6). We resort to both numerical and analytical methods to estimate these costs.

A. Numerical estimates

Computing the likelihood requires estimating the normalization constant Z in Eq. (2). Since the exact calculation of Z is intractable we use the annealed importance sampling (AIS) algorithm [47]. AIS estimates Z through a number of intermediate ‘annealed’ distributions interpolating between the original RBM distribution and a simpler independent model that can be exactly sampled. This procedure provides a stochastic upper bound on the likelihood, which converges to the true value as the number of interpolating distribution increases. A stochastic lower bound can be obtained by a reverse interpolation procedure [48], which gradually ‘melts’ the independent model back into the target RBM; see SI for details. Combining the two bounds sandwiches the true likelihood value and ensures that sampling has converged.

Results are shown for the three datasets considered in this work in the top row of Figure 8. We measure the likelihood costs for making labels inaccessible to linear discriminators based on the RBM representations (red bars or dots). In all datasets the labels considered are relevant

to the nature of the data, and the costs (per data configuration) induced by the constraints on the weights are significant: $\Delta\mathcal{L}_{\text{part. erasure}} \simeq 12$ for MNIST0/1, $\simeq 750$ for the two-dimensional Ising model ($\beta = 0.44$, $L = 64$), and $\simeq 5.6$ for bacteria/eukaryotic KH protein sequences.

The relation between label relevance and the likelihood cost is nicely portrayed in the two-dimensional Ising model dataset. At low β , the data is essentially random and the magnetization is mostly irrelevant to determining the probability of a configuration. In this regime, erasing label information has little likelihood cost. As the inverse temperature increases, the magnetization becomes more relevant, and it becomes necessary for the model to account for it to achieve good likelihood. In consequence, partially erasing the magnetization in this regime results in a large likelihood loss.

The top row of Figure 8 furthermore shows the values of the log-likelihoods after releasing one hidden unit (blue bars and dots). The log-likelihood loss with respect to the unconstrained RBM, $\Delta\mathcal{L}_{\text{rel.}}$ in Eq. (12) is guaranteed to be non-negative. In practice, for the MNIST0/1 and Ising model datasets, we estimate this cost to be small ($\Delta\mathcal{L}_{\text{rel.}} \simeq 8$ and $\simeq 0$, respectively), and somewhat larger for the KH domain ($\simeq 2.4$). This is consistent with the ability of the released RBM to fit and generate high-quality data in the three cases, as shown in previous sections.

B. Analytical estimates

We can gain some analytical insights about the origin of the costs of partial erasure and of disentanglement as follows. To make our RBM models mathematically tractable we now assume that the visible and hidden units of the RBM are all real valued and Gaussianly distributed, with the exception of a single spin-like hidden unit, $h_1 = \pm 1$ (intended to be eventually released to help concentrating label-related information). This RBM model defines a bimodal Gaussian mixture distribution, with two modes associated to the label classes $u = \pm 1$, see Figure 9A & B.

The energy function under this Gaussian-Spin RBM model (GS) writes,

$$E_{\text{GS}}(\mathbf{v}, \mathbf{h}) = \sum_i \frac{v_i^2}{2\sigma_i^2} - \sum_i g_i v_i + \sum_{\mu \geq 2} \frac{h_\mu^2}{2} - \sum_i \sum_{\mu \geq 2} w_{i\mu} v_i h_\mu - \sum_i w_i^* v_i h_1 \quad (27)$$

where the σ_i ’s parametrize the standard deviations of the visible units, and the visible units are connected to the Gaussian hidden units through the weights $w_{i\mu}$, and to the spin hidden unit through w_i^* .

We first train the RBM in the absence of any constraint on the weights. The data are characterized by their empirical correlation matrix, \mathbf{C} , and the vector $\mathbf{q}^{(1)}$

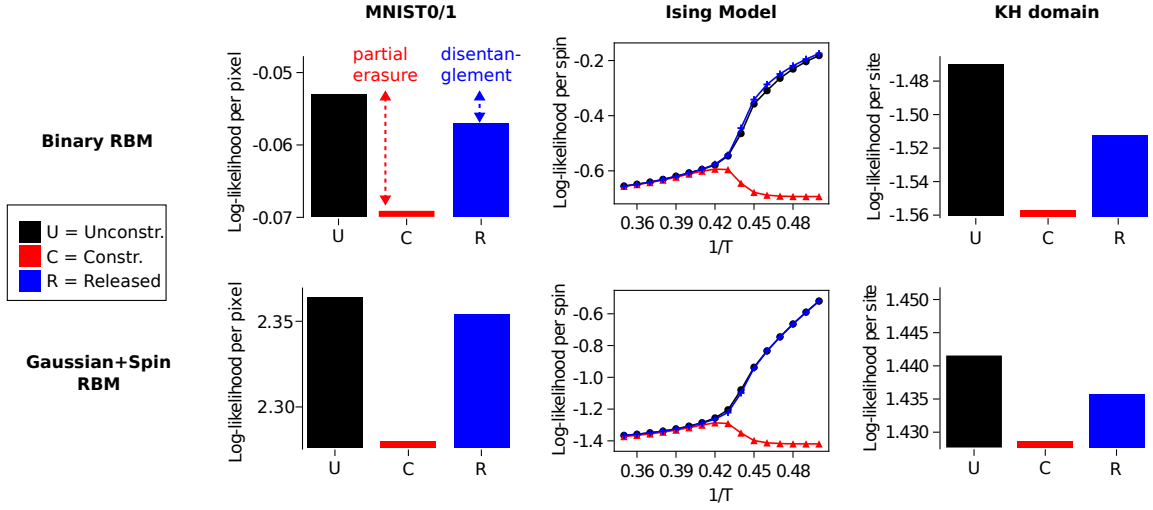


FIG. 8. **Likelihood calculations.** First row shows numerical estimates of the log-likelihood using RBMs with binary hidden units, along with the costs of applying (6) partially or on the full hidden layer. Bottom row shows analytical results obtained in an RBM with one hidden spin unit and the remaining Gaussian hidden units (Figure 9). First column shows the legend: Black for the unconstrained model, red for models with all hidden units constrained, and blue for models with the constraint acting on all but one hidden unit. Subsequent columns show the results for the three datasets considered: MNIST0/1, two-dimensional Ising model, and the KH protein domain. The discontinuous arrows in the first panel highlight the likelihood costs of partial label erasure (red) and disentanglement (blue).

separating the center of masses between the classes, see Figure 2C. Maximizing the likelihood of the data gives several conditions over the weight vectors that we list below:

1. The scaled weights $w_{i\mu}\sigma_i$ for $\mu \geq$ are eigenvectors of the matrix $\tilde{\mathbf{C}} = \mathbf{D}(\mathbf{C} - \mathbf{q}^{(1)}(\mathbf{q}^{(1)})^\top)\mathbf{D}$, with corresponding eigenvalues $\lambda_\mu = 1/(1 - \sum_i w_{i\mu}^2 \sigma_i^2)$; here \mathbf{D} is the diagonal matrix with entries $1/\sigma_i^2$. In practice, the top $M - 1$ eigenvalues of $\tilde{\mathbf{C}}$ (larger than unity) have to be selected to maximize the likelihood.
2. The weights \mathbf{w}^* onto hidden unit $\mu = 1$ are given by $\Sigma^{-1}\mathbf{q}^{(1)}$, where $\Sigma = (\mathbf{D} - \mathbf{W}\mathbf{W}^\top)^{-1}$ denotes the covariance matrix predicted by the model, and \mathbf{W} is the matrix of weight vectors $w_{i\mu}$ with $\mu \geq 2$.
3. The biases on the visible units are such that the model fits the independent site frequencies: $\mathbf{g} = \Sigma^{-1}(\langle \mathbf{v} \rangle_{\mathcal{D}} - \mathbf{q}^{(1)})$.

Details about the derivation can be found in SI. The likelihood reads

$$\mathcal{L}_{\text{GS}} = \frac{1}{2} \sum_{\mu} (\lambda_{\mu} - 1 - \log \lambda_{\mu}) - \log \cosh(\mathbf{g}^\top \mathbf{q}^{(1)}) \quad (28)$$

where the λ_{μ} 's are the selected eigenvalues of $\tilde{\mathbf{C}}$, and we have ignored irrelevant additive terms.

We next consider maximum likelihood training of a RBM in the presence of orthogonality constraints acting on the Gaussian weights, while w_i^* is unconstrained, see

Eq. (6). Let us define the projection operator onto the subspace orthogonal to $\mathbf{q}^{(1)}$,

$$\mathbf{P} = \mathbb{I} - \frac{\mathbf{q}^{(1)}(\mathbf{q}^{(1)})^\top}{(\mathbf{q}^{(1)})^\top \mathbf{q}^{(1)}}. \quad (29)$$

It is easy to realize that conditions (6) are equivalent to $\mathbf{P}\mathbf{W} = \mathbf{W}$. Consequently the discussion of the unconstrained learning case above applies to the constrained case provided the correlation matrix $\tilde{\mathbf{C}}$ is replaced with the projected matrix $\tilde{\mathbf{C}}^\perp = \mathbf{P}\tilde{\mathbf{C}}\mathbf{P}$.

The eigenvalues of the projected matrix $\tilde{\mathbf{C}}^\perp$ have a precise ordering relationship to the eigenvalues of the original matrix $\tilde{\mathbf{C}}$, known as Poincaré separation theorem (see Theorem 11.11 of [21]). Denoting by $\lambda_1, \dots, \lambda_N$ the eigenvalues of the original matrix, and by $\lambda_1^\perp, \dots, \lambda_N^\perp$ the eigenvalues of the projected matrix, both ranked in decreasing order, we have

$$\lambda_1 \geq \lambda_1^\perp \geq \lambda_2 \geq \lambda_2^\perp \geq \dots \geq \lambda_N \geq \lambda_N^\perp = 0, \quad (30)$$

where $\lambda_N^\perp = 0$ is due to the forbidden direction $\mathbf{q}^{(1)}$, which results in a drop of the rank of the matrix. Moreover, the gaps $\lambda_i - \lambda_i^\perp$, are connected to the angle between the forbidden direction $\mathbf{q}^{(1)}$ and the eigenvectors of the original correlation matrix. Figure 9C shows a low-dimensional example, in which a 3-dimensional ellipsoid symbolizing $\tilde{\mathbf{C}}$ is projected to the space orthogonal to one of the vectors shown. We consider two vectors with different angles to the ellipsoid principal axis, which define the projected ellipse $\tilde{\mathbf{C}}^\perp$.

The likelihood of the released Gaussian-Spin RBM is given by the same formula as for the unconstrained

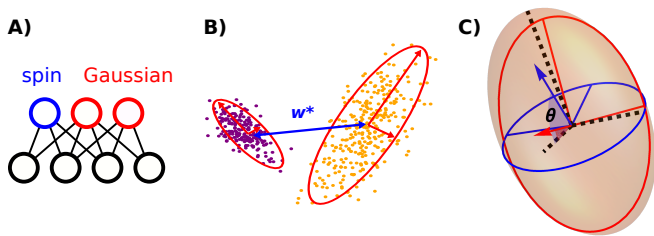


FIG. 9. **Gaussian-Spin RBM.** A) The Gaussian-Spin RBM has one spin-like hidden unit, $h_1 = \pm 1$, whereas all other hidden units are Gaussian. B) The spin hidden unit (blue) separates the two labelled classes. Gaussian hidden units (red) model intra-class variability. C) Illustration of Poincaré theorem.

model, see Eq. (28), upon replacement $\lambda_\mu \rightarrow \lambda_\mu^\perp$. As the function is monotonous in the eigenvalues (when they are larger than unity) Poincaré separation theorem in Eq. (30) guarantees that the likelihood decreases when imposing the constraints on the weights.

Lastly, when the orthogonality constraint (6) acts on all weights, the model is blind to the separation of the classes. We obtain the likelihood of the constrained RBM by simply replacing $\mathbf{q}^{(1)}$ in the above calculation with the zero vector, and consequently $w_i^* = 0$ also.

The bottom row of Figure 8 shows the log-likelihoods estimates produced by this approximate calculation in the unconstrained, constrained and released cases. While the absolute values of the log-likelihoods cannot be directly compared to the binary RBM settings, we see that the relative changes from unconstrained to constrained, associated to the partial erasure cost, and from constrained to released, defining the disentanglement cost fairly match their counterparts computed by annealed importance sampling on Binary RBMs.

VIII. DISCUSSION

In this work, we have studied the ability of RBMs to extract disentangled representations from data and exploit these to generate samples with desired properties.

This goal has been pursued in the literature [7–9, 11] with deep neural networks, with predominant approaches being based on Variational Auto-Encoders [3, 49] and adversarial networks [4, 7, 11]. Despite the broad success of adversarial learning and its importance in practical applications [7], the aforementioned methods suffer from the following drawbacks: Deep neural networks are difficult to interpret and require large amounts of data to train. Variational auto-encoders [3] enforce a continuous mapping of the data to a Gaussian distribution, which is not always suitable, for instance if the data consist of separated peaks [50]. Finally adversarial training suffers from instabilities that are not yet well-understood, making the training difficult to implement in practice.

Our approach exploits the RBM: a simple two layer

network which may be more suitable when few data are available. When RBM is trained under appropriate conditions, such as regularization and appropriate potentials on the hidden units, it learns interpretable weights [18], directly reflecting key features of the data; finally RBM can be considered as the building blocks of deeper networks.

While classification from the hidden units activity can be achieved with a normal RBM, disentanglement is difficult and necessary for generation in a particular class. Here we use the simple RBM structure to derive explicit disentanglement constraints that can be applied directly on the RBM weights during learning. These constraints are derived from the requirement that the data representations corresponding to different classes, are approximately indistinguishable from the inputs on the constrained hidden units. More precisely, we impose linear and quadratic constraints on the RBM weights that decorrelate the class label from the hidden unit activities. As in the adversarial framework, imposing these constraints on only a subset of hidden units, allows us to manipulate the samples generated from the model by controlling the state of the remaining hidden units.

The resulting training algorithm is easily implementable and fast (pseudocode in SI), being based on two steps: First, we estimate the required constraints from labeled data. Crucially, this is the only step that requires labels. Second, we train the RBM following standard practice [51], but after each gradient update, we modify the weights to project them into the space satisfying the constraints. The resulting procedure has similar computational cost as normal RBM training. It is therefore robust, not suffering from instability due to the maximization-minimization of the cost function used in traditional adversarial learning. Moreover it does not need to have labels for all data: once the constraints have been determined, the RBM training step can exploit unlabeled data (see SI for an example).

The linear (quadratic) constraints we have derived here, achieve exact removal of label information from the representation, only in the case of Gaussian data with labels generated by a linear (quadratic kernel) (see the theorem in SI). For other data distributions, or more complex labels, these constraints achieve a partial erasure, and we have shown that the label can still be recovered, but requiring more complex discriminator machines (*e.g.*, Figure 4B). In spite of this limitation, constraining subsets of hidden units appears to be sufficient to manipulate representations and produce data with desired features.

We have demonstrated the effectiveness of this approach on three datasets from diverse domains: the MNIST collection of handwritten digit images [22], the Ising model from statistical physics, and protein sequences of the KH domain family [23]. MNIST is a popular benchmark in machine-learning and the labels are straightforwardly associated to the digit identities. On this dataset, we have shown that RBM can be trained to associate one or few controlling hidden units to each digit

class, which can be manipulated to sample and transition between classes.

The two-dimensional Ising model is a very well-studied system in statistical physics, with a precisely characterized phase transition depending on external parameters and the temperature. Standard RBM is able to learn the behavior of interesting observables, such as magnetization, heat capacity, susceptibility, and correlation length. We then imposed a linear constraint on the weights (see (6)), decorrelating the latent representation from the magnetization sign, and forcing the RBM to hallucinate a new system with interesting physical properties. Remarkably, although the constrained RBM is unable to generate magnetized configurations, it preserves the structure of correlations between spins, as evident from second-order observables such as the heat capacity and correlation length. Through an heuristic argument we proposed a Hamiltonian to describe the physical properties of this system, containing a non-analytic penalty term for the global magnetization, reminiscent of non-analytic Landau potentials recently proposed to describe non-equilibrium steady states of the Ising magnet [52–54]. Releasing a single hidden unit then restores the ability of the model to generate magnetized configurations, reproducing all statistics of the original Ising model.

Our last application is in protein design, based on model learning from sequence-data, a field which has grown of importance in bio-engineering since the recent impressive developments of sequencing technologies [55]. RBM trained on the K homology domain family under linear constraints decorrelating a subset of hidden inputs from the taxonomy of sequences, efficiently concentrate taxonomic information in a control hidden unit. Conditional sampling reproduces the fine statistical differences

of the eukaryotic and bacterial sub-families. The transition between the two classes, happens on a shorter time than the overall decorrelation time, suggesting that sequences might be able to change class while maintaining a memory of other, class-independent attributes.

Nothing guarantees that concentrating an important feature of the data into one or few hidden units of the RBM is not detrimental to the ability of the model to fit the data. It is conceivable that complex features might require encoding through several hidden units. Consequently, we estimated the log-likelihood cost of partial erasure and disentanglement in the three datasets. The cost of partial erasure is related to the relevance of the label, as clearly illustrated in the dependence on temperature in the Ising model data. On the other hand, disentanglement in the three cases is achieved with a small likelihood loss, evidencing the robustness of the approach. If the data can be approximated as a mixture of two Gaussians, we have shown how the log-likelihood losses can be calculated analytically, and established a connection between the likelihood costs, and the Poincaré separation theorem.

In summary, our work complements the existing literature on unsupervised learning of disentangled representations, with a simple effective framework, amenable to approximate analytical calculations.

The codes needed to reproduce the results reported in this work are available on Github.

ACKNOWLEDGMENTS

J. FdCD, S.C., R.M. are supported by the ANR-17 RBMPro CE30-0021-01 and ANR-19 Decrypted CE30-0021-01 grants.

-
- [1] Y. Bengio, Deep learning of representations for unsupervised and transfer learning, in *Proceedings of ICML workshop on unsupervised and transfer learning* (JMLR Workshop and Conference Proceedings, 2012) pp. 17–36.
 - [2] R. Salakhutdinov and G. Hinton, Deep boltzmann machines, in *Artificial intelligence and statistics* (PMLR, 2009) pp. 448–455.
 - [3] D. P. Kingma and M. Welling, Auto-encoding variational bayes, arXiv preprint arXiv:1312.6114 (2013).
 - [4] I. J. Goodfellow, J. Pouget-Abadie, M. Mirza, B. Xu, D. Warde-Farley, S. Ozair, A. Courville, and Y. Bengio, Generative adversarial networks, arXiv preprint arXiv:1406.2661 (2014).
 - [5] W. J. Johnston, S. E. Palmer, and D. J. Freedman, Non-linear mixed selectivity supports reliable neural computation, *PLOS computational biology* **16**, e1007544 (2020).
 - [6] F. Locatello, S. Bauer, M. Lucic, G. Raetsch, S. Gelly, B. Schölkopf, and O. Bachem, Challenging common assumptions in the unsupervised learning of disentangled representations, in *international conference on machine learning* (PMLR, 2019) pp. 4114–4124.
 - [7] G. Lample, N. Zeghidour, N. Usunier, A. Bordes, L. Denoyer, and M. Ranzato, Fader networks: Manipulating images by sliding attributes, arXiv preprint arXiv:1706.00409 (2017).
 - [8] H. Kim and A. Mnih, Disentangling by factorising, in *International Conference on Machine Learning* (PMLR, 2018) pp. 2649–2658.
 - [9] Q. Hu, A. Szabó, T. Portenier, P. Favaro, and M. Zwicker, Disentangling factors of variation by mixing them, in *Proceedings of the IEEE Conference on Computer Vision and Pattern Recognition* (2018) pp. 3399–3407.
 - [10] B. Esmaeili, H. Wu, S. Jain, A. Bozkurt, N. Siddharth, B. Paige, D. H. Brooks, J. Dy, and J.-W. Meent, Structured disentangled representations, in *The 22nd International Conference on Artificial Intelligence and Statistics* (PMLR, 2019) pp. 2525–2534.
 - [11] Z. He, W. Zuo, M. Kan, S. Shan, and X. Chen, Attgan: Facial attribute editing by only changing what you want, *IEEE transactions on image processing* **28**, 5464 (2019).
 - [12] Y. Shen, J. Gu, X. Tang, and B. Zhou, Interpreting the

- latent space of gans for semantic face editing, in *Proceedings of the IEEE/CVF Conference on Computer Vision and Pattern Recognition* (2020) pp. 9243–9252.
- [13] J. Zaidi, J. Boilard, G. Gagnon, and M.-A. Carboneau, Measuring disentanglement: A review of metrics, arXiv preprint arXiv:2012.09276 (2020).
- [14] C. Feutry, P. Piantanida, Y. Bengio, and P. Duhamel, Learning anonymized representations with adversarial neural networks, arXiv preprint arXiv:1802.09386 (2018).
- [15] R. Zemel, Y. Wu, K. Swersky, T. Pitassi, and C. Dwork, Learning fair representations, in *International conference on machine learning* (PMLR, 2013) pp. 325–333.
- [16] M. Arjovsky and L. Bottou, Towards principled methods for training generative adversarial networks, arXiv preprint arXiv:1701.04862 (2017).
- [17] G. E. Hinton, A practical guide to training restricted boltzmann machines, in *Neural networks: Tricks of the trade* (Springer, 2012) pp. 599–619.
- [18] J. Tubiana, S. Cocco, and R. Monasson, Learning protein constitutive motifs from sequence data, *Elife* **8**, e39397 (2019).
- [19] B. Bravi, J. Tubiana, S. Cocco, R. Monasson, T. Mora, and A. M. Walczak, Rbm-mhc: A semi-supervised machine-learning method for sample-specific prediction of antigen presentation by hla-i alleles, *Cell systems* **12**, 195 (2021).
- [20] R. Salakhutdinov, A. Mnih, and G. Hinton, Restricted boltzmann machines for collaborative filtering, in *Proceedings of the 24th international conference on Machine learning* (2007) pp. 791–798.
- [21] K. M. Abadir and J. R. Magnus, *Matrix algebra*, Vol. 1 (Cambridge University Press, 2005).
- [22] L. Deng, The MNIST database of handwritten digit images for machine learning research, *IEEE Signal Processing Magazine* **29**, 141 (2012).
- [23] S. El-Gebali, J. Mistry, A. Bateman, S. R. Eddy, A. Luciani, S. C. Potter, M. Qureshi, L. J. Richardson, G. A. Salazar, A. Smart, *et al.*, The pfam protein families database in 2019, *Nucleic acids research* **47**, D427 (2019).
- [24] R. J. Baxter, *Exactly solved models in statistical mechanics* (Elsevier, 2016).
- [25] D. Yevick and R. Melko, The accuracy of restricted boltzmann machine models of ising systems, *Computer Physics Communications* **258**, 107518 (2021).
- [26] M. Harsh, J. Tubiana, S. Cocco, and R. Monasson, ‘place-cell’ emergence and learning of invariant data with restricted boltzmann machines: breaking and dynamical restoration of continuous symmetries in the weight space, *Journal of Physics A: Mathematical and Theoretical* **53**, 174002 (2020).
- [27] T. M. Cover, *Elements of information theory* (John Wiley & Sons, 1999).
- [28] A. Engel and C. Van den Broeck, *Statistical mechanics of learning* (Cambridge University Press, 2001).
- [29] N. Brenner, W. Bialek, and R. d. R. Van Steveninck, Adaptive rescaling maximizes information transmission, *Neuron* **26**, 695 (2000).
- [30] B. Scholkopf and A. J. Smola, *Learning with kernels: support vector machines, regularization, optimization, and beyond* (MIT press, 2018).
- [31] V. A. Marchenko and L. A. Pastur, Distribution of eigenvalues for some sets of random matrices, *Matematicheskii Sbornik* **114**, 507 (1967).
- [32] L. Onsager, Crystal statistics. i. a two-dimensional model with an order-disorder transition, *Physical Review* **65**, 117 (1944).
- [33] M. E. Newman and G. T. Barkema, *Monte Carlo methods in statistical physics* (Clarendon Press, 1999).
- [34] N. Yoshioka, Y. Akagi, and H. Katsura, Transforming generalized ising models into boltzmann machines, *Physical Review E* **99**, 032113 (2019).
- [35] G. Cossu, L. Del Debbio, T. Giani, A. Khamseh, and M. Wilson, Machine learning determination of dynamical parameters: The ising model case, *Physical Review B* **100**, 064304 (2019).
- [36] W. Selke, Critical binder cumulant of two-dimensional ising models, *The European Physical Journal B-Condensed Matter and Complex Systems* **51**, 223 (2006).
- [37] K. Shimagaki and M. Weigt, Selection of sequence motifs and generative hopfield-potts models for protein families, *Physical Review E* **100**, 032128 (2019).
- [38] D. Sehnal, S. Bittrich, M. Deshpande, R. Svobodová, K. Berka, V. Bazgier, S. Velankar, S. K. Burley, J. Koča, and A. S. Rose, Mol* viewer: modern web app for 3d visualization and analysis of large biomolecular structures, *Nucleic Acids Research* **49**, W431 (2021).
- [39] N. V. Grishin, Kh domain: one motif, two folds, *Nucleic acids research* **29**, 638 (2001).
- [40] B. M. Lunde, C. Moore, and G. Varani, Rna-binding proteins: modular design for efficient function, *Nature reviews Molecular cell biology* **8**, 479 (2007).
- [41] R. Valverde, L. Edwards, and L. Regan, Structure and function of kh domains, *The FEBS journal* **275**, 2712 (2008).
- [42] G. Musco, G. Stier, C. Joseph, M. A. C. Morelli, M. Nilges, T. J. Gibson, and A. Pastore, Three-dimensional structure and stability of the kh domain: molecular insights into the fragile x syndrome, *Cell* **85**, 237 (1996).
- [43] W. T. O’Donnell and S. T. Warren, A decade of molecular studies of fragile x syndrome, *Annual review of neuroscience* **25**, 315 (2002).
- [44] T. U. Consortium, UniProt: the universal protein knowledgebase in 2021, *Nucleic Acids Research* **49**, D480 (2020), <https://academic.oup.com/nar/article-pdf/49/D1/D480/35364103/gkaa1100.pdf>.
- [45] S. Cocco, C. Feinauer, M. Figliuzzi, R. Monasson, and M. Weigt, Inverse statistical physics of protein sequences: a key issues review, *Reports on Progress in Physics* **81**, 032601 (2018).
- [46] F. Morcos, A. Pagnani, B. Lunt, A. Bertolino, D. S. Marks, C. Sander, R. Zecchina, J. N. Onuchic, T. Hwa, and M. Weigt, Direct-coupling analysis of residue coevolution captures native contacts across many protein families, *Proceedings of the National Academy of Sciences* **108**, E1293 (2011).
- [47] R. Neal, Annealed importance sampling (technical report 9805 (revised)), Department of Statistics, University of Toronto (1998).
- [48] Y. Burda, R. Grosse, and R. Salakhutdinov, Accurate and conservative estimates of mrf log-likelihood using reverse annealing, in *Artificial Intelligence and Statistics* (PMLR, 2015) pp. 102–110.
- [49] I. Higgins, L. Matthey, A. Pal, C. Burgess, X. Glorot, M. Botvinick, S. Mohamed, and A. Lerchner, Beta VAE: Learning basic visual concepts with a constrained variational framework, *ICLR* (2016).

- [50] S. Goldt, B. Loureiro, G. Reeves, F. Krzakala, M. Mézard, and L. Zdeborová, The gaussian equivalence of generative models for learning with shallow neural networks, in *Mathematical and Scientific Machine Learning* (PMLR, 2022) pp. 426–471.
- [51] T. Tieleman, Training restricted boltzmann machines using approximations to the likelihood gradient, in *Proceedings of the 25th international conference on Machine learning* (2008) pp. 1064–1071.
- [52] D. Belitz, T. Kirkpatrick, and T. Vojta, How generic scale invariance influences quantum and classical phase transitions, *Reviews of modern physics* **77**, 579 (2005).
- [53] C. Aron and M. Kulkarni, Nonanalytic nonequilibrium field theory: Stochastic reheating of the ising model, *Physical Review Research* **2**, 043390 (2020).
- [54] C. Aron and C. Chamon, Landau theory for non-equilibrium steady states, *SciPost Physics* **8**, 074 (2020).
- [55] H. T. Rube, C. Rastogi, S. Feng, J. F. Kribelbauer, A. Li, B. Becerra, L. A. Melo, B. V. Do, X. Li, H. H. Adam, *et al.*, Prediction of protein–ligand binding affinity from sequencing data with interpretable machine learning, *Nature Biotechnology* , 1 (2022).